Defense Technical Information Center
Compilation Part Notice

ADP012075

TITLE: Developed Cavitation-Cavity Dynamics

DISTRIBUTION: Approved for public release, distribution unlimited

This paper is part of the following report:

TITLE: Supercavitating Flows [les Ecoulements supercavitants]

To order the complete compilation report, use: ADA400728

The component part is provided here to allow users access to individually authored sections of proceedings, annals, symposia, etc. However, the component should be considered within the context of the overall compilation report and not as a stand-alone technical report.

The following component part numbers comprise the compilation report:
ADP012072 thru ADP012091

Developed Cavitation-Cavity Dynamics

David R. Stinebring
Michael L. Billet
Jules W. Lindau
Robert F. Kunz
Applied Research Laboratory
P.O. Box 30
State College, PA 16804
USA

Introduction

When we discuss high-speed supercavitating bodies, it primarily involves the fully developed supercavitating phase. For many cases the body must transition from fully wetted, through the partially cavitating regime before reaching supercavitation. Therefore, an understanding of all phases of cavitation is necessary.

Flow regimes and basic definitions

Cavitating flows are commonly described by the cavitation number, σ, expressed as

$$\sigma \equiv \frac{P - P_v}{\frac{1}{2}\rho V^2} \tag{1}$$

where, P and V are the reference pressure and velocity, respectively, P_v is the vapor pressure at the bulk temperature of the liquid, and ρ is the mass density of the liquid. If a cavitation experiment is conducted by holding the velocity constant and varying the reference pressure, various amounts of cavitation can be observed as shown in Figure (1). Noncavitating flows occur at sufficiently high pressures where there is no evidence of bubbles. Supercavitation occurs at very low pressures where a very long vapor cavity exists and in many cases the cavity wall appears glassy and stable except near the end of the cavity. Between these flow regimes is limited cavitation and developed cavitation.

V & P₁   Noncavitating Flow

$\sigma > \sigma^i$ DECREASING PRESSURE

V & P₂   Cavitation Inception or
Limited Cavitation

$\sigma \leq \sigma^i$

V & P₃   Developed Cavitation

$\sigma << \sigma^i$

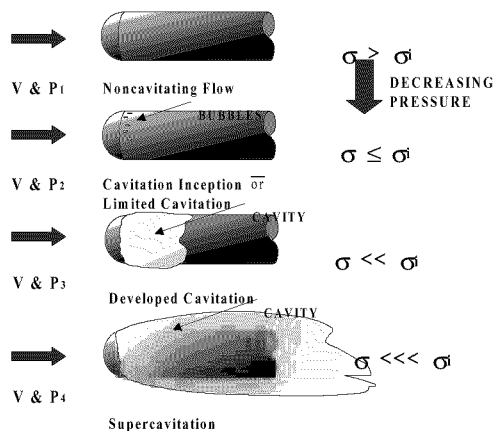V & P₄   Supercavitation

$\sigma <<< \sigma^i$

Figure 1: Schematic of cavitation flow regimes

Limited cavitation occurs at an intermediate value of the cavitation number where amount of a given type of cavitation is minimized. Limited cavitation can be vaporous or gaseous. The former type of cavitation is caused by the explosive growth of bubbles due to the rapid conversion of liquid to vapor at the bubble wall whereas the latter is due to a slower mode of bubble growth caused by the transport of noncondensible gas into the bubble. The condition at which cavitation initially appears is called cavitation inception.

Of particular importance in the study of cavitation is the minimum pressure coefficient, $C_{p_{min}}$ given by

$$C_{p_{min}} = \frac{p_{min} - P}{\frac{1}{2}\rho V^2}$$ (2)

where, P_{min} is the minimum pressure in the liquid. The "classical theory for scaling vaporous limited cavitation" states that, $\sigma = -C_{p_{min}}$ and $C_{p_{min}} = $ constant. This implies that when scaling from one flow state to another, the characteristics of the flow field and its boundaries remain geometrically and kinematically similar. However, real flows often do not obey the classical theory because of so-called "scale effects" which arise from changes in velocity, size, fluid properties and microbubble distribution. Experimental results clearly show that in many cases, the limited cavitation number can be greater or less than the minimum pressure coefficient and in some cases the minimum pressure coefficient is not constant, such as in vortical flows. One example of scale effects can be noted from the "standard" cavitation tests conducted at many facilities for the ITTC. Figure (2) shows some of the cavitation data and the varied appearance of the cavitation data can be noted in Figure (3).
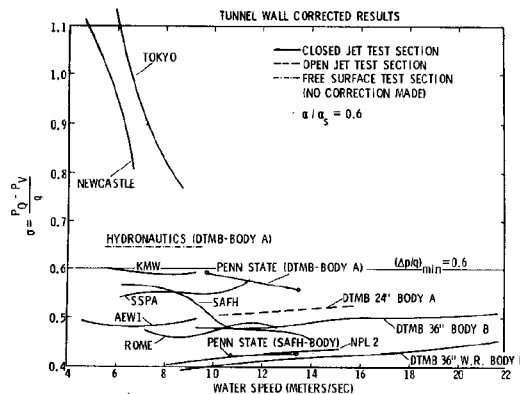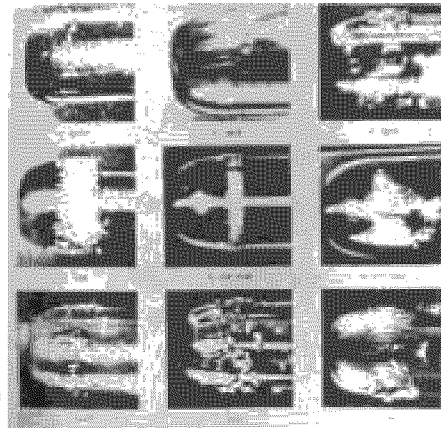

Figure 2: ITTC cavitation data

Figure 3: Photographs of cavitation appearance for ITTC data

Extensive research has been conducted into scale effects, such as in References (1), (2), and (3). Also, it is very important to determine the definition of limited cavitation when comparing experimental results. In general, these studies into scale effects can be divided into two general types as follows:

Viscous Effects: Scale effects that act on the flow outside the cavitation bubble which influence the local pressure in the liquid flow.

1. Flow field changes due to variations in Reynolds number, Froude number, and Mach number including steady and turbulent pressure fluctuations.

2. Departures from exact geometric similarity such as those due to roughness and manufacturing.

Bubble Dynamic Effects: Scale   effects that act on the bubble growth process which cause the liquid pressure at the cavitation bubbles to depart from the equilibrium vapor pressure corresponding to the bulk temperature of the liquid.

1. Time effects.

2. Heat transfer effects.

3. Surface tension effects

4. Transport of noncondensible gas

5. Liquid tension, i.e., microbubbles.

The various factors which causes scale effects and the influence on the cavitation number can be ascertained by employing the Rayleigh-Plesset equation to describe the growth of a "typical" cavitation bubble. This equation can be written as

$$\rho\left(R\ddot{R}+\frac{3}{2}\dot{R}^2\right)=P_G(t)-\frac{2S}{R}-\frac{4\mu\dot{R}}{R}-\left[C_p(t)+\sigma+C_T(t)\right]\frac{1}{2}\rho V^2 \tag{3}$$

where,

$$C_p(t)=\frac{P(t)-P}{\frac{1}{2}\rho V^2}$$

and,

$$C_T(t)=\frac{P_v(T)-P_v(T_r(t))}{\frac{1}{2}\rho V^2}.$$

Thus $C_p(t)$ is the time varying pressure coefficient which describes the variation of the liquid pressure outside of the bubble. The thermodynamic coefficient (C_T) describes the effect of heat transfer on the vapor pressure in the bubble. The term $\overline{P_G}$ is the partial pressure of gas inside the bubble and the term $\frac{2\overline{S}}{R}$ is the "liquid" tension of the bubble. Multiplying Equation (3) by a time interval (dt), integrating over a time interval (T_c) which is typical of a cavitation process, and solving for σ yields

$$\sigma=-\overline{C}_p+\frac{\overline{P_G}}{\frac{1}{2}\rho V_\infty^2}-\frac{\frac{2\overline{S}}{R}}{\frac{1}{2}\rho V_\infty^2}-\phi-\overline{C}_T \tag{4}$$

where, ϕ is a bubble dynamic parameter. The bars denote averages over the interval T_C. In the absence of significant dynamic effects, Equation (4) reduces to an equilibrium equation

$$\sigma=-\overline{C}_p+\frac{\overline{P_G}-\frac{2\overline{S}}{R}}{\frac{1}{2}\rho V^2}-\overline{C}_T \tag{5}$$

Referring to Equation (5), it is noted that the terms P_G, $\dfrac{2\overline{S}}{R}$, and C_T all cause bubble dynamic scale effects and the liquid tension effect and thermodynamic coefficient will reduce the cavitation number at inception and the gas pressure in the bubble will increase the cavitation number at inception. Viscous scale effects are contained with the average pressure coefficient $\overline{C}_p$. This can be written as

$$-\overline{C}_p = -\overline{C}_{p_s} + \frac{\overline{\nabla P}_T}{\frac{1}{2}\rho V_\infty^2} + \frac{\overline{\nabla P}_R}{\frac{1}{2}\rho V_\infty^2} + \frac{\overline{\nabla P}_U}{\frac{1}{2}\rho V_\infty^2}$$

where $\overline{C}_{p_R}$ is the average local pressure in the absence of surface roughness $\left(\overline{\Delta P}_R\right)$, turbulence, $\left(\overline{\Delta P}_T\right)$ and flow unsteadiness $\left(\overline{\Delta P}_U\right)$.

Scale effects are very important in understanding the physics of cavitation. They are important as can be noted in Figure (4) for a Schiebe headform and in Figure (5) for a 1/8-caliber ogive. Figure (6) shows the effect of boundary layer transition on limited cavitation.
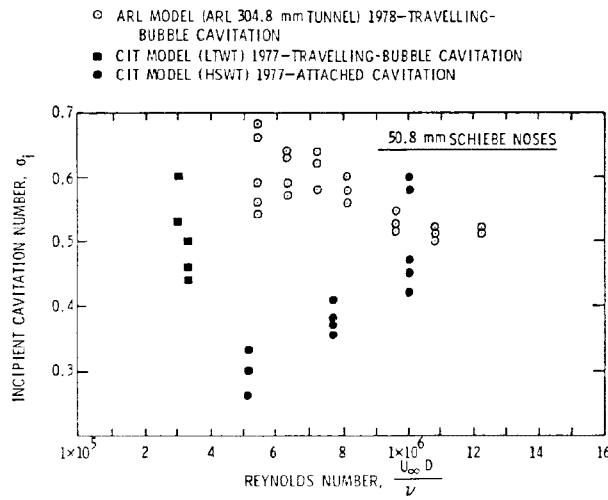

Figure 4: Comparison of CIT and ARL Penn State inception data for 50.8-mm (2.0-inch) Schiebe noses
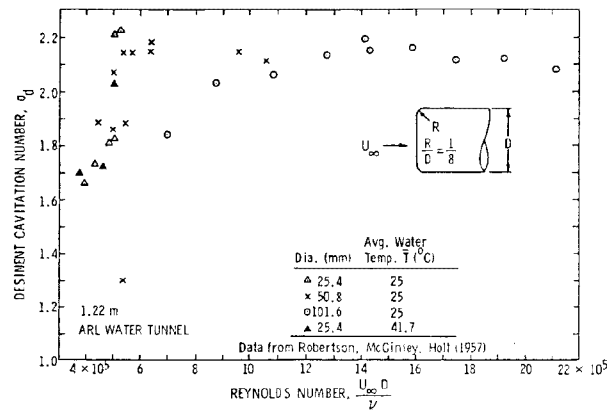

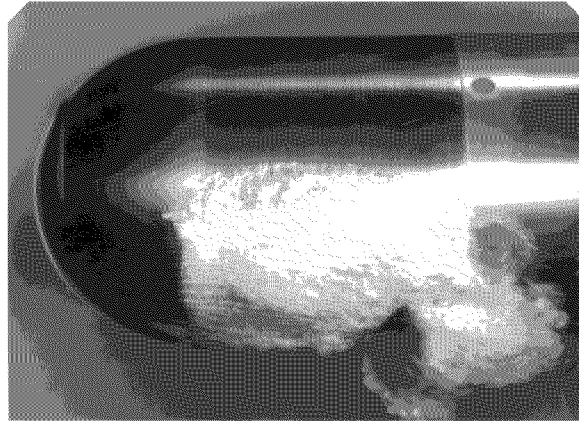Figure 5: Desinent cavitation number versus Reynolds number for 1/8-caliber ogives

Figure 6: Effect of boundary layer transition on limited cavitation

Developed Cavitation

The subject of a fully developed cavity and the various similarity laws which predict the cavity parameters have been studied by many researchers and some of these results are discussed in other lectures. However, this research has largely been divided into two types of cavity flows: (1) ventilated cavities, and (2) vaporous cavities. These cavities have been shown to have one similar characteristic in that the cavity shape is a single-valued function of the cavitation number based on cavity pressure. Thus, the cavitation number for developed cavitation is based on cavity pressure (P_c) and can be expressed as

$$\sigma = \frac{P - P_c}{\frac{1}{2}\rho V_\infty^2}$$
(6)

where $P_c \approx P_V + P_G - \Delta P_V$ for vaporous cavity and P_c would be P_{VE} for the ventilated cavity. The rear of these cavities is a complex and often highly turbulent region of the flow where the contents of the cavity are carried or entrained away. However, in the case of vaporous cavitation where the cavity contains mostly vapor, the loss of vapor is immediately made up by the evaporation from the walls of the cavity. On the other hand, a continual supply of gas is needed to form a ventilated cavity.

Fluid properties of the liquid inherently affect the vaporization process along the cavity wall, which supplies vapor to the cavity in a similar manner as is the case of limited cavitation. This scale effect is given the term "thermodynamic effect," and is noted by the effect of liquid temperature variation on the cavitation number. It is the same as for limited cavitation and it will become more significant as the temperature is increased, resulting in the cavity temperature being lower than the bulk temperature of the fluid. One of the first theoretical and experimental investigations into the variation of cavitation number with temperature has been conducted by Stahl and Stepanoff[4]. A detailed investigation into this effect was conducted by Holl, Billet, and others at Penn State that developed the entrainment theory[5],[6]. This investigation provides insite into the characteristics of developed cavitation.

Most of this thermodynamic scale effect investigation used a zero-caliber-ogive body shown in Figure (7). At small cavity lengths (L/D < 2.0), the cavity is very cyclic and the re-entrant jet formed at the cavity closure strikes the leading edge of the cavity. The photograph of the cavity on the zero-caliber ogive was taken with continuous lighting so the cavity appears like seen to the naked eye. Figures (8 to 11) show cavity behavior seen with high-speed movies and very short-duration strobe flash lighting. The unsteady nature of the cavity is apparent. Observing the cavitation with continuous lighting provides a time average view of the cavity, which also can lead to problems in investigating developed cavitation.

The cavity length is a measure of the cavitation number. However, determination of the cavity length visually is subjective, since an observer is seeing a time average of the cavity, and pressure measurements are affected by the transient nature of the cavity.
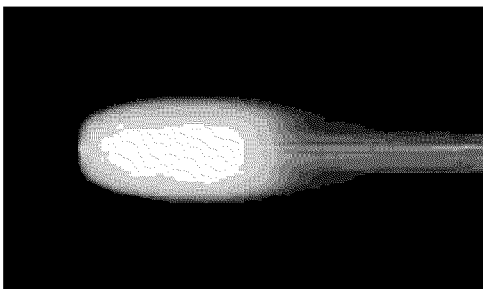

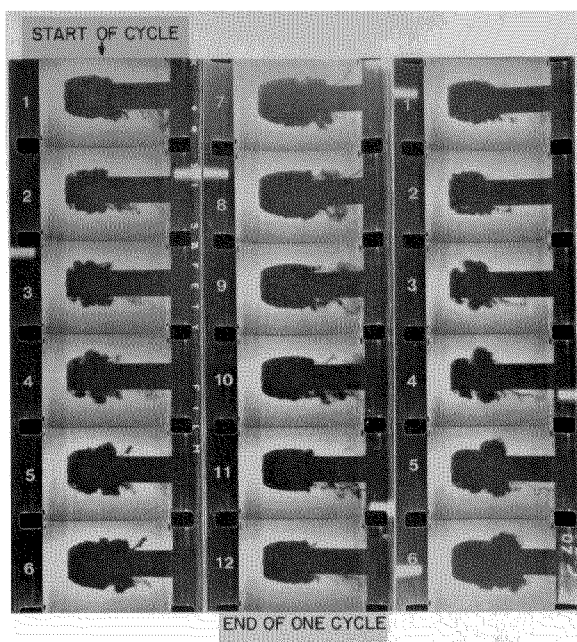Figure 7: Photograph of cavity on a zero-caliber ogive illuminated with continuous lighting

Figure 8: Sequence from a high-speed movie showing a complete cavity cycle- 5000 frames per second- 6.35-mm (0.25-inch) diameter zero-caliber ogive, Velocity = 25 m/sec

Figure 9: Detail of cavity after reentrant jet strikes leading edge, first image in sequence is below

Figure 10: Photograph of cavity on zero-caliber ogive illuminated with a 3-μ sec flash
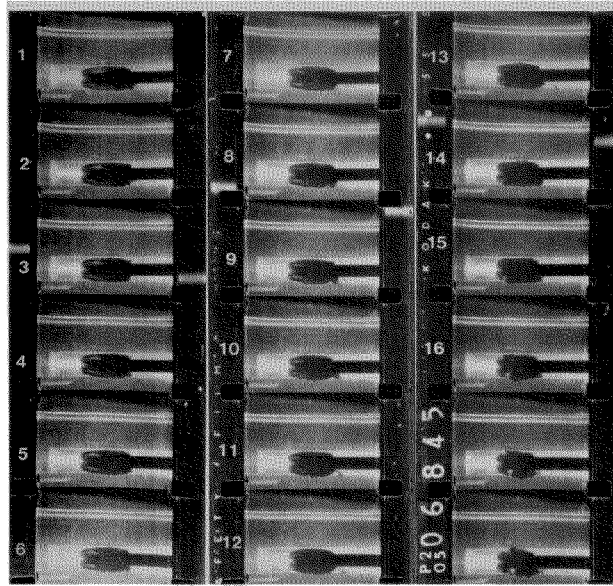

Figure 11: Sequence from high-speed movie showing the reentrant jet moving through the cavity and striking the cavity leading edge (between frames 11 and 12)- 5000 frames per second- 6.35-mm (0.25-inch) diameter zero-caliber ogive, Velocity = 15 m/sec

The high-speed movie sequences show that the unsteady nature of the cavities is due to the reentrant jet moving through the cavity and striking the cavity leading edge. This causes the cavity to detach from the cavitator leading edge and break into helical vortices connected by vortex filaments, Figures 9 and 10.

The cavity on the zero-caliber ogive is similar to the bubble shape of the wake associated with the separated flow from the model nose. At the end of this bubble there is a re-entrant jet and the velocity of this jet of liquid can be expressed as

$$V_j = V(1 + \sigma)^{\frac{1}{2}} \tag{7}$$

which can be derived from Bernoulli's equation which assumes that the frictionless fluid. This condition is similar to the vortical flow near the end of the wake bubble. At appropriate values of Reynolds numbers a regular vortex sheet is observed in the wake region aft of bubble closure. At higher Reynolds numbers a turbulent wake with irregular mixing results. For the case of the cavity closure on the body, the re-entrant travels along the body surface to the cavity separation location.

As the re-entrant jet affects the cavity dynamics, the body experiences a time dependent drag. Gilbarg and Serrin[7] show that this change of drag can be related to the momentum of the re-entrant jet and hence a characteristic dimension of this jet.

Measurements made inside of a developed cavity also indicate the physics of the vaporization process. As shown in Figure (12), the maximum temperature depression from inside the cavity indicating that most of the vaporization process is occurring near the beginning of the cavity where the curvature is greatest. This maximum temperature depression is affected by the air content of the liquid as shown in Figure (13). Consequent measurement of the cavity pressure indicates that this is due to the presence of noncondensible gas (partial pressure above vapor pressure). The magnitude of the pressure unsteadiness that occurs in the cavity as shown in Figure (14). This is due to the re-entrant jet.

The geometric characteristics of developed cavities were determined from a series of experiments conducted by Billet and Weir[5],[6]. From measurements of the cavity profiles, the maximum cavity diameter (D_m), cavity half-length (A), and cavity surface area were determined for both natural and ventilated cavities. Data shows that for a given model geometry and cavitation number, ventilated and natural cavities have the same profile, within experimental error. This was found to be independent of reference velocity, and cavity dimension are directly proportional to the model diameter as shown in Figure (15). This is in agreement with several other investigators such as Wade[9].
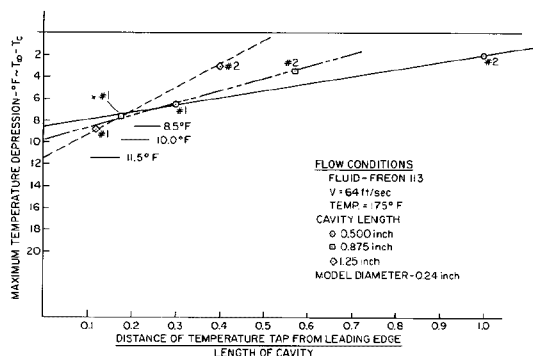

Figure 12: Maximum temperature depression versus cavity tap position for Freon 113; Temperature= 175° F, L= 0.50, 0.875, and 1.25-inch, V=64 ft/sec
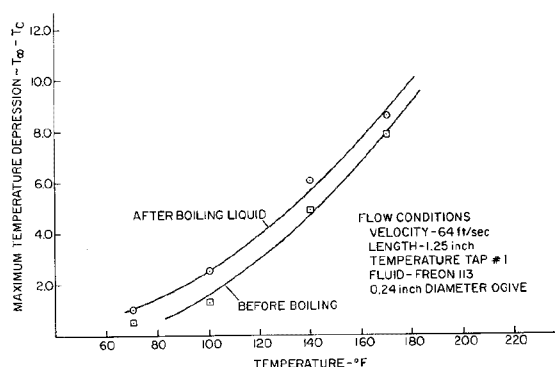

Figure 13: Cavity temperature depression versus temperature for Freon 113, V=19.5 m/sec, L=3.18 cm (1.25-inch), two different air contents
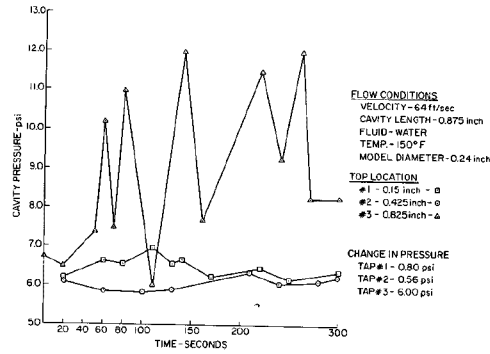
Figure 14: Cavity tap pressures versus time for water; temperature= 66° C,
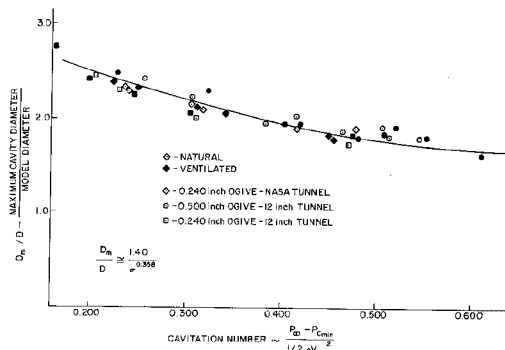L= 2.2 cm (0.875-inch), V=19.5 m/sec

Figure 15: Ratio of maximum cavity to model diameter versus corrected cavitation number

For ventilated cavities, the flow coefficient is defined as

$$C_Q = \frac{Q}{VD^2} \qquad (8)$$

where Q is the ventilation rate and D is the reference dimension. This is a dimensional representation of the volume flow rate of gas needed to sustain a cavity. This volume flow rate is the same regardless if it is a ventilated or vapor cavity. This assumption is supported by Reichardt, who demonstrates that the drag and geometry for similar vaporous and ventilated cavities are the same.

One of the first experimental investigations of air entrainment was carried out at the California Institute of Technology in 1951 by Swanson and O'Neill[10]. In their experiments an air filled cavity was maintained behind a 2.54-cm disk over a cavitation number range of 0.25 to 0.08 and a corresponding Froude number range of 10 to 15. Their results show that as the supply of air to the ventilated cavity was decreased from a maximum flow coefficient of 1.6, the cavity size decreased only slightly over a large range of air supply rates until a certain minimum rate of air supply was reached. Thereafter, a slight decrease in the air supply led to a rapid reduction in the size of the cavity for small values of flow coefficients.

In the region where the cavity size varies rapidly with the flow coefficient, the cavity has a re-entrant jet closure. A further increase in flow coefficient causes the re-entrant jet to break down and be replaced by the twin-vortex regime. This demonstrates the existence of two distinct flow coefficient regions which are determined by the cavity closure conditions.

An extensive analysis of the various factors which influence air entrainment for ventilated cavities in the twin-vortex regime is presented by Cox and Clayden[11]. They show theoretically that high rates of air entrainment are associated with the formation of the twin-vortex system. They also present experimental data for ventilated cavities on 2.54-, 1.91-, and 1.27-cm-diameter disks which show that for a given rate of air entrainment, the cavity length to disk diameter ratio increases as the Froude number based on disk diameter increases.

Waid[12] also measured flow coefficients for ventilated cavities on a series of three-dimensional hydrofoils. The results obtained for both the re-entrant jet and two-vortex regimes show the same trends as the data obtained by Swanson and O'Neill[10].

Gas diffusion was found to have a significance on the cavity pressure (above vapor pressure) and on the measured thermodynamic effect. Thus, the entrainment rate needed to sustain a natural cavity has contributions not only from the vapor but also from gas diffusion. Gas diffusion was also found to have a significant effect on the gas needed to sustain a ventilated cavity. Billet and Weir[13] conducted an experimental investigation into this effect. An analysis of this effect was conducted based on a mathematical model of diffusion developed by Brennen[14].

Gas diffusion will occur when there exists a concentration gradient between the freestream and the cavity. This concentration gradient can be calculated from the partial pressures of the gas. The maximum partial pressure of the gas in the freestream can be determined from a knowledge of the air content and Henry's Law

$$P_{FS} = \alpha \cdot \beta \tag{9}$$

where, α is the air content in   ppm by moles and β is Henry's Law constant, which depends on temperature. The mass flow rate of diffused gas into the cavity is proportional to the concentration gradient and can be expressed in terms of the difference in partial pressures as

$$M_{DG} = f(\text{transport}) \left[P_L \frac{P_{FS} - P_G}{\beta} \right] \tag{10}$$

where, f(transport) is a dimensional function of the parameters influencing the diffusion mechanism and P_G is the partial pressure of noncondensible gas in the cavity. This transport function can be determined from a knowledge of the free shear layer over the cavity surface. A schematic of this process is shown in Figure (16) from Brennen[14].
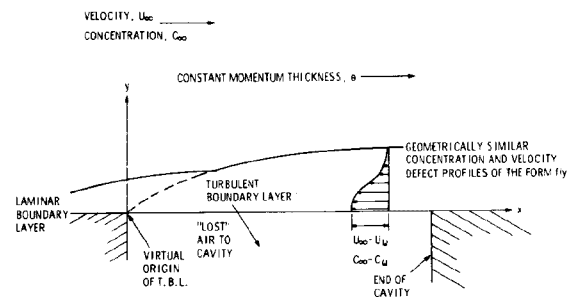

Figure 16: Schematic for an undersaturated cavity (Brennen [14])

The results of this analysis are shown in Figure (17). In this figure, the effect on flow coefficient is given for both an undersaturated and oversaturated condition. These data were then corrected for gas diffusion effects and compare favorably to the data for no gas diffusion.
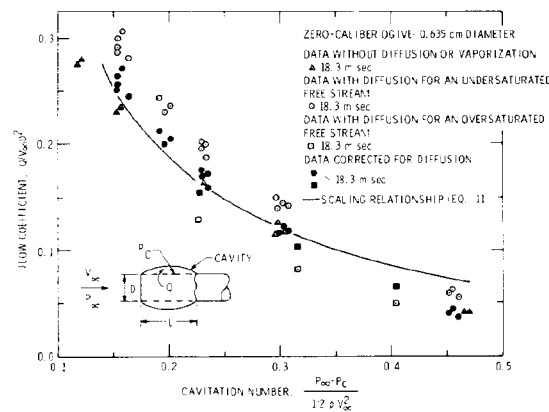

Figure 17: Flow coefficient data with diffusion for 6.35-mm diameter zero-caliber ogive, V= 18.3-m/sec

Supercavitation

When a cavity length is much greater than the body dimensions, this flow regime is described as supercavitation. The cavity stays attached to the body and the cavity closure is far downstream. The length of the cavity does not vary significantly even though considerable oscillations can occur at its closure. However, the cavity acts as if it were an extension of the body. In this case, the same flow field would exist around a solid body having a shape comprising of the wetted nose plus the free-cavity profile. Unlike developed cavities, the gross features of supercavitation on a headform are not only functions of the cavitation number but also the Froude number-gravity becomes important.

Supercavities have many characteristics of classical free streamline flows. The cavity interior is essentially at constant pressure, and the cavity walls are essentially free-stream surfaces of constant velocity. Cavity pressures approach vapor pressure. These assumptions are the basis of many theoretical treatments of cavity geometry and forces. Many of these theories will be presented during this course; however, only cavity dynamics will be discussed in this section.

There exists a transition between the re-entrant jet closure condition and the twin-vortex closure condition. This has been discussed in many previous investigations. However, a study of water-entry modeling by Stinebring and Holl[15] describes this transition of flow regimes in detail and will be discussed briefly.

It has been observed that for a ventilated cavity there exists a condition when the cavity length for a given flow condition suddenly grows to four or five times its original length with only a slight increase in the ventilation air flow rate. This instability in the cavity length may be attributed to the transition between the re-entrant jet and twin-vortex flow regimes.

Previous discussions on developed cavitation are for flows where gravity effects are not important and the re-entrant jet is the gas entrainment mechanism. However, at low velocities or longer cavity lengths and gravity is normal to the flow, the cavity will move upward to the body centerline as a result of buoyancy. The flow velocities of the top surface of the cavity will be different than on the lower surface, which will result in a net circulation. As a result, a new cavity equilibrium system is established where entrainment now occurs through the vortex cores of the twin-vortex structure at cavity closure.

A photograph of the cavity in the re-entrant jet regime is shown in Figure (18). The conical nose is supported by support struts so the aft region the cavity can be investigated with minimum disturbance. The opaque appearance of the cavity is primarily due to the violent mixing caused by the re-entrant jet. As transition to the twin-vortex regime takes place, the cavity becomes clear at the leading edge but with some mixing due to the re-entrant jet. The photograph in Figure (19) shows the cavity in the twin vortex regime. This transitional region between flow regimes was also observed for models which have afterbodies (sting mounted) although this effect was not as pronounced. The full growth of the cavity could not be realized because of interference at the downstream end of the cavity.
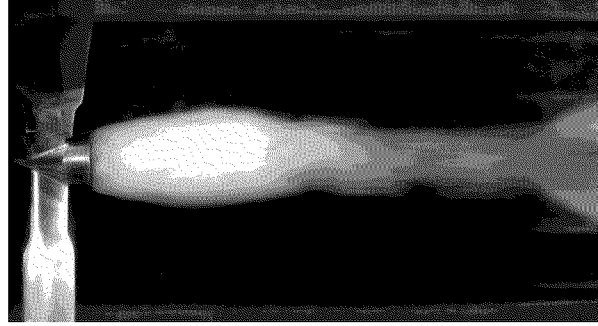

Figure 18: Photograph of cavity for a 45° conical nose illuminated with continuous lighting
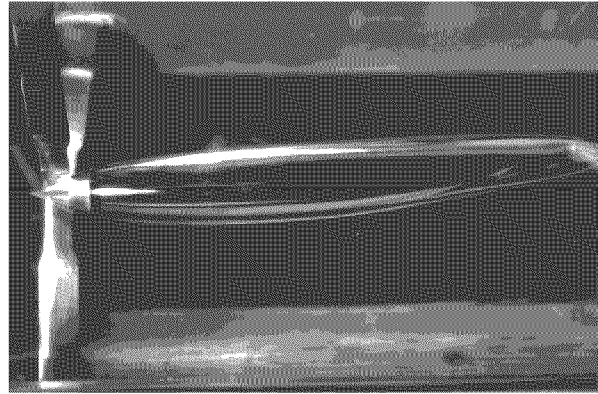

Figure 19: Photograph of twin vortex cavity downstream of a strut-mounted 45° cone

Cavitator hydrodynamics

For supercavitating flow the cavitator is located at the forward most location on the body, and the cavity downstream of the cavitator covers the body. The shape of the cavity is defined by the cavitation number based on cavity pressure. The simplest form of cavitator is a disk where the drag coefficient is defined as,

$$C_d = 0.82(1+\sigma). \tag{11}$$

There have been numerous expressions derived for cavity dimensions as a function of cavitation number. Reichardt (16) showed that the cavity length divided by the cavity diameter is independent of the shape of the cavitator and is only a function of cavitation number,

$$\frac{L}{d_m} = \frac{\sigma + 0.008}{\sigma(0.066 + 1.7\sigma)}. \tag{12}$$

Reichardt also developed an expression for the cavity diameter divided by the cavitator diameter,

$$\frac{d_m}{d} = \left(\frac{C_d}{\sigma - 0.132 \sigma^{8/7}} \right)^{0.5} ,$$ (13)

which is only a function of cavitation number and cavitator drag coefficient, C_d.

By substituting the definition of drag coefficient into equation (13) and rearranging, the drag force required to create an axisymmetric cavity of a given diameter is:

$$D_{cavity} = \frac{\pi}{8} \rho \, V_\infty^2 \, d_m^2 \, (\sigma - 0.132 \, \sigma^{8/7})$$ (14)

where, ρ is the mass density of the fluid. For a given velocity and cavity diameter, the drag is only a function of the cavitation number. It is not a function of the geometry of the cavitator.

The shape of the cavity is approximately elliptical. A number of researchers have developed formulas for the cavity, most notably, Logvinovich (17). The cavity radius is given as,

$$R = R_k \sqrt{1 - \left(1 - \frac{R_1^2}{R_k^2} \right)\left(1 - \frac{t}{t_k} \right)^{\frac{2}{\chi}}}$$ (15)

where, R_k, is the maximum cavity radius, t_k, is the time of formation to the cavity midpoint, χ, is a correction factor, $\chi = 0.85$, and R_1 and t are the radius and time of formation at the matching station, x_1, where,

$$t = \frac{x - x_1}{V_k}$$

and where, x, is the streamwise distance, and V_k, is the cavitator velocity.

Since there is a gas filled cavity over the body, there is a loss of buoyancy so the body must be supported by contact with the cavity wall. The cavitator must be at an angle of attack to provide lift to support the forward section of the body, and the aft section can be supported by the afterbody planing or control surfaces or a combination of both. The cavity shape will be influenced by foreshortening due to the cavitator at angle of attack, and perturbations due to downwash from lift and bouyancy effects. These effects upon the cavity shape are beyond the scope of this paper and are covered in Logvinovich.

Experimental facilities and test programs

These next sections will briefly cover some of the facilities and test programs at ARL Penn State related to cavity dynamics, cavity ventilation requirements, cavitator testing, and control surface testing. They are intended to show the hardware and techniques that have been used to investigate the physics of developed cavitation.

Testing Facilities at ARL Penn State

The Garfield Thomas Water Tunnel of the Applied Research Laboratory Penn State is a complex of hydrodydynamic and hydroacoustic test facilities that are registered with the International Towing Tank Conference, an organization of member counties that design and test ships and other marine structures in tanks and tunnels. Since the 48-inch Diameter Water Tunnel began operation in 1949, many additional facilities and capabilities were added. Many of the smaller water tunnels are utilized to research specific physics problems, so it is especially appropriate for graduate student work.

Three facilities are specially utilized for supercavitation studies and are: (1) 48-inch Diameter Water Tunnel, (2) 12-inch Diameter Water Tunnel, and (3) Ultra-High-Speed Cavitation Tunnel. The 12-inch Diameter Water Tunnel was built in 1951 and the Ultra-High-Speed Cavitation tunnel was built in 1962. These three facilities will be discussed briefly.

48-INCH (1.22 M) DIAMETER WATER TUNNEL (GARFIELD THOMAS WATER TUNNEL)

This large water tunnel is a variable –speed, variable-pressure tunnel primarily intended for propulsion studies of body-propulsor systems. It is a closed circuit, closed-jet water tunnel. A detailed description of the facility is given in Figure (20).

The tunnel has two honeycombs in the 3.66 m diameter "settling section" to not only straighten the flow, but also reduce the test section turbulence level below 0.1 percent. The cylindrical working section is four feet in diameter and 4.27 m long. The water velocity in the working section is variable up to 24.4 m/sec. And is controlled by a four-bladed, adjustable pitch impeller which is 2.41 m in diameter and is driven by a 1491 kW electric motor.

The pressure in the working section may be reduced to 20.7 kPa, which permits a wide range of cavitation numbers for testing. The air content of the water in the tunnel is controlled through the use of a degasser that permits removal of air from the water. Thus, the water in the working section can be less than air-saturated regardless of the working section.

The degassing system is located in the tunnel by-pass system, which also has filters and the tunnel pressure control systems. This by-pass can handle from 500 gpm to 3000 gpm from the tunnel and can be operated during cavitation testing to remove air and bubbles. Gas removal from the water is accomplished with a Cochrane Cold-Water Degasifier. This degasser consists of an upright cylindrical tank where the upper portion is filled with plastic saddles. Water taken from the tunnel is sprayed into the top of the tank, the interior being maintained at a high vacuum. The water spray falling over the saddles exposes a thin water film to a vacuum, which permits the rapid removal of air. The water collects at the bottom of the degasser and is returned to the bypass system.

CAVITATION TUNNEL (GARFIELD THOMAS) 1949
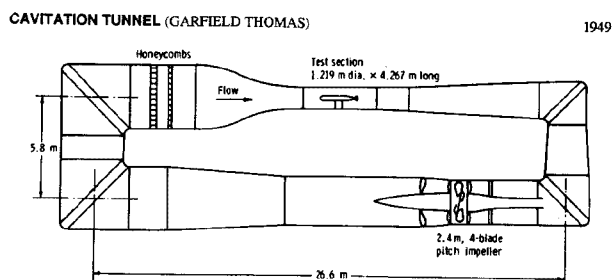
Description of Facility: Closed Circuit, Closed Jet

Type of Drive System:4-Blade Adjustable Pitch Impeller

Total Motor Power:2000 HP Variable Speed (1491 kW)

Working Section Max. Velocity: 18.29 m/s

Max. & Min. Abs. Pressures:413.7 to 20.7 kPa

Cavitation number Range:>0.1 dependent on velocity and/or J-range

Instrumentation: Propeller dynamometers, five-hole probes, pitot probes, lasers, pressure sensors, hydroplanes, planar motion mechanism, force balances.

Type and Location of Torque & Thrust Dynamometers: Model internally mounted, 150 hp limit (111.85 kW).

Propeller or Model Size Range: Model size from 76.2 mm to 635.0 mm id.

Tests Performed: Forces, flow field, and pressure distributions on bodies of revolution, hydrofoils, propellers, etc. Cavitation performance and noise measurements of propellers, foils, hydrodynamic shapes, etc. Steady state and time-dependent force and torque measurements on powered models. Flow visualization.

Other Remarks: Tunnel turbulence level is 0.1 percent in test section. Air content can be controlled as low as 1 ppm per mole. Measurement can be made of hydrodynamic functions for stability and control of submerged vehicles. Directional hydrophone system for relative acoustic measurements.

Published description: ARL Penn State Report NORD 16597-56, Lehman, 1959.

Applied Research Laboratory, Fluid Dynamics Department, The Pennsylvania State University, USA

Figure 20: Description of the ARL Penn State 48-inch diameter water tunnel

12-INCH (0.305 M) DIAMETER WATER TUNNEL

The facility is typically used for flow studies that do not require wake-operating propellers. This is a closed-circuit tunnel, which has the similar working section velocity and pressure range as the Garfield

Thomas Water Tunnel. As is the case of other facilities, the pressure is independent of the working section velocity and details are given in Figure (21),

One of the unusual features of this facility is the use of two interchangeable working sections for different test purposes. A circular section is 0.305 m in diameter, and a rectangular one is 0.51 m high and 11.4 cm wide; each is 0.76 m long. The circular working section is used to study the bodies employed in three-dimensional flow problems. The rectangular one is to study hydrofoils and slots and other two-dimensional flow problems.

The tunnel drive consists of a mixed-flow pump that forms a part of the lower leg and one turn of the tunnel circuit. The pump is driven by a 150 hp electric induction motor through a variable-speed fluid coupling and reducing gear. The method of cooling the tunnel water is by a heat exchanger, which is an integral part of the circuit.

The tunnel is also connected to the by-pass circuit of the 48-inch diameter water tunnel so that the air content and free air can be controlled.

CAVITATION TUNNEL   1951
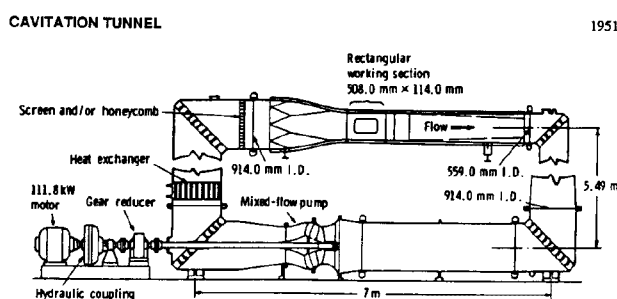
Description of Facility: Closed Circuit, Closed Jet

Test Sections:(1) Circular: 304.8 mm dia x 762.0 mm long

(2) Rectangular: 508.0 mm x 114.3 mm x 762.0 mm long

Type of Drive: Mixed Flow Peerless Pump

Total Motor Power: 150 hp (11.8 kW)

Working Section Max. Velocity:24.38 m/s

Max. & Min. Abs. Pressures: 413.7 to 20.7 kPa

Cavitation Number Range:>0.1 dependent on velocity

Instrumentation:Lasers, pressure sensors, hydrophones

Model Size Range:50.8 mm max. dia.

Tests Performed: Steady and time-dependent force and pressure measurements on unpowered models. Noise measurements on cavitating models. Three-dimensional flow problems (circular section). Two-dimensional flow problems (rectangular section). Axial-flow pump tests.

Other Remarks: Independent gas control of air content. Water filtration with 25-micrometer filters. Intermittent operation with drag-reducing additive injection. Partial neutralization of additive downstream of test section.

Published Description: ARL Penn State Report NORD 16597-56, Lehman, 1959.

Figure 21: Description of the ARL Penn State 12-inch diameter water tunnel

ULTRA-HIGH-SPEED CAVITATION TUNNEL

Much of the basic studies on cavitation have been conducted in the Ultra-High-Speed Cavitation Tunnel. The characteristics of this tunnel are given in Figure (22).

This tunnel is a high-speed, high-pressure system which is designed so that the velocity in the test section can be varied from 13.7 to 100 m/sec. The tunnel pressure can be varied to a maximum of 8.3 MPa. The inside diameter of the test section of 3.81 cm.

The entire tunnel circuit is made of stainless steel except for the lucite test section windows and the bronze centrifugal pump. The small amount of corrosion in the system coupled with a bypass filtering circuit allows for a very clean system.

The bearing for the centrifugal pump shaft is lubricated by drawing water from the tunnel circuit through the bearing and thus this method of lubrication avoids possible contamination which would be encountered in a system employing hydrocarbon lubricants. As the fluid leaves the bearing, it enters an accumulator tank and from there is pumped by means of a triplex pump back to the tunnel. Pressure control is obtained by by-passing a portion of the fluid from the discharge of the triplex pump to the accumulator tank and/or bleeding some fluid from the main tunnel circuit. A surge tank is located in the pressure control circuit in order to remove fluctuations caused by the triplex pump. The liquid in the tunnel by-pass is filtered down to remove particles above two microns.

Also, a 14 kw heater is located in the by-pass circuit. It has the capability to heat the liquid to temperatures in excess of 176°C. Water, Freon 113, and alcohol have been used as working fluids in this facility.

ULTRA-HIGH SPEED CAVITATION TUNNEL   1960
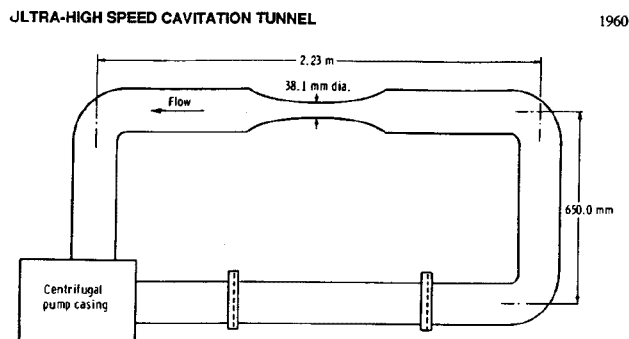
Description of Facility:Closed Circuit, Closed Jet

Type of Drive System:Centrifugal Variable Speed Drive

Total Motor Power: 75 hp (55.9 kW)

Working Section Max. Velocity: 83.8 m/s

Max. & Min. Abs. Pressures:8274.0 to 41.4 kPa

Cavitation Number Range:>0.01 dependent on velocity and velocity

*Instrumentation:*Pressure and temperature sensors, lasers

Temperature Range:16°C to 176°C

Model Size Range:12.7 mm max. dia.

Test Medium:Water, Freon 113, Alcohol

Tests Performed: Incipient and desinent cavitation studies. Development cavittion studies. Cavitation damage.

Other Remarks: Stainless steel tunnel. Bronze pump. Three filter banks for removal of water, acides, solid particles (10 micrometers) depend on fluid media.

Published Description: ARL Penn State TM 75-188, Weir, Billet & Holl, 1975.

Figure 22: Description of the ARL Penn State 1.5-inch diameter water tunnel

Measurements of cavity dynamics in the reentrant flow regime

As stated previously, if the product of the cavitation number and Froude number is above a critical value, then the cavity will be in the reentrant flow regime. The oscillation of the cavity in the reentrant regime affects the ventilation gas entrainment and the body dynamics. Therefore, understanding the dynamics of reentrant jet cavities is important.

A 45° conical-nosed model having a 2.54-cm (1.0- inch) diameter afterbody was instrumented with an internally mounted piezoelectric transducer, Figure 23. It was expected that the reentrant jet striking the cavity would cause a significant pressure rise that could be measured with the transducer. Spectral analyses were performed on the transducer output to determine the frequency of the cavity cycling. Tests were conducted with both vaporous and ventilated cavities over a range of cavitation numbers and

velocities of 9.1, 13.7 and 15.2 m/sec (30, 45, and 50 ft/sec). High-speed movies of the cavitation were taken and compared to the spectrum analyzer results. To determine if the boundary layer thickness affects the cycling frequency, a number of tests were conducted with distributed roughness applied to the conical nose. Lastly, the results were compared with the findings of previous investigations in water tunnels covering a wide range of model sizes and geometries.
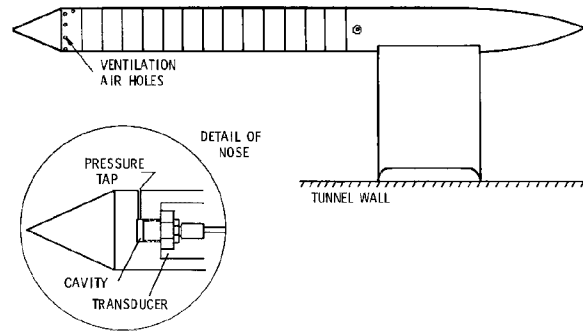

Figure 23: Schematic of model for measuring cavity cycling showing the location
of the pressure transducer (inset)

The cavity cycling frequency Strouhal number based on body diameter is defined as

$$S = \frac{fD}{V_\infty}$$

where, f is the cycling frequency, and D is the body diameter. A plot of cycling frequency Strouhal number as a function of cavitation number is presented in Figure (24).   The data of Knapp (18) for hemispherical nosed models and from Stinebring (8) for zero caliber ogives are also shown in the figure. The trend of lower cycling frequency for lower cavitation numbers, i.e., larger cavities, is the same for all models for vaporous and ventilated cavities. The Strouhal number can also be defined such that the characteristic length scale is the ratio of cavity length to model diameter, L/D. A plot of Strouhal number as a function of L/D is presented in Figure (25).   The plot shows that the cavity length is the characteristic dimension for cavity cycling and that the Strouhal number based on cavity length is a constant, approximately, $S = 0.16$.
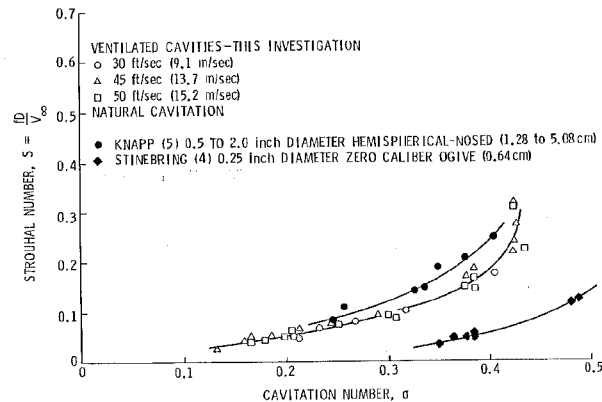

Figure 24: Cavity cycling Strouhal number, based on body diameter, as a function of cavitation number for vaporous and ventilated cavities for a number of investigations having different test geometries
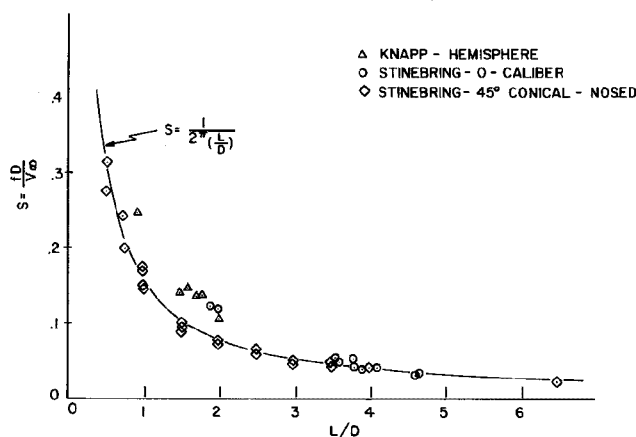
Figure 25: Cavity cycling Strouhal number, based on cavity length divided by body diameter, as a function of cavity length divided by body diameter for vaporous and ventilated cavities for a number of investigations having different test geometries

Effect of afterbody shape upon gas entrainment

Since most of the gas entrainment takes place in the aft region of a body, the afterbody shape should affect the required ventilation rate to generate a cavity. Tests were performed in the ARL Penn State 0.305-m (12-inch) diameter water tunnel to examine afterbody effects upon gas entrainment. The models used for this study are shown in Figure (26). Each model had a 25.4-mm (1.0-inch) diameter 45° apex angle conical nose. One model had a 25.4-mm (1.0-inch) afterbody, the second had a 12.7-mm (0.5-inch) afterbody, and the third model was supported by three struts and had no afterbody. All models had six holes for introduction of ventilation gas and a pressure tap for measuring cavity pressure. Tests were conducted at velocities of 9.1, 13.7, and 15.2-m/sec (30, 45, and 50 ft/sec). To minimize gaseous diffusion across the cavity wall, the test conditions were selected so the cavity pressure was close to the partial pressure of gas in the surrounding water.
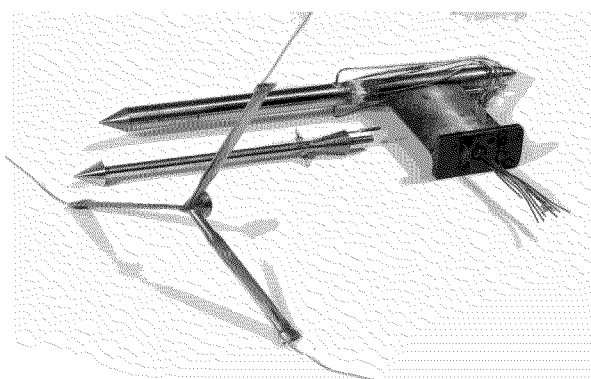

Figure 26: Photograph of the models used to examine the effect of afterbody on gas entrainment

The results of the study for a tunnel velocity of 13.7- m/sec (45-ft/sec) are displayed in Figure (27). The model requiring the lowest flow rate for a given cavitation number was the one with no afterbody. The model having the afterbody one-half of the cone diameter required the largest ventilation flow rate (except at the highest cavitation numbers), and the model with the afterbody equal to the cone diameter

was between the two. It would seem that the model with no afterbody should require the largest flow rate, because of the greater volume of gas inside the cavity, but this was not the case. The reentrant jet behavior could possibly account for this effect. Observations show that gravity causes the reentrant jet to move along the bottom of the cavity for the model with no afterbody. An afterbody causes a "guiding effect" upon the reentrant jet that results in more mixing at the top of the cavity. It is not known why the smaller afterbody required the largest ventilation. The data does show that afterbody design is important to minimize ventilation requirements.
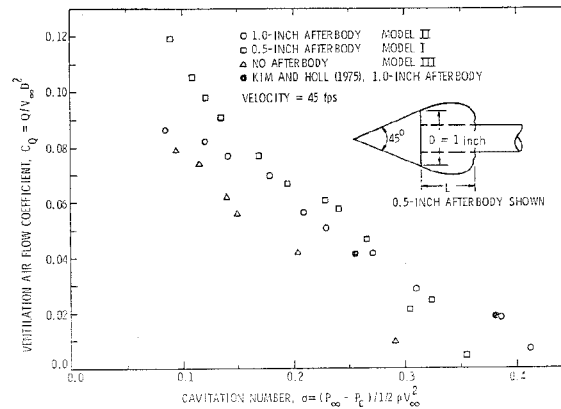
Figure 27: The effects of afterbody arrangement on ventilation requirements

Cavitator testing

A photograph of a model for cavitator testing in the ARL Penn State 12-inch diameter water tunnel is shown in Figure (28). The models can incorporate systems for introducing ventilation gas, cavitator force balances, pressure measurement systems, and other instrumentation. Just downstream of the cavitator in the figure is a gas deflector that redirects the gas flow to minimize disturbances to the cavity. The strut-mounted model is attached to the large dark plate, which is the section that mounts to the water tunnel test section. A typical mounting, for a cavitator at angle of attack, to a force balance, is shown in Figure (29). Care must be taken to ensure that the design for the introduction of ventilation gas does not have a significant effect upon the force measurements.
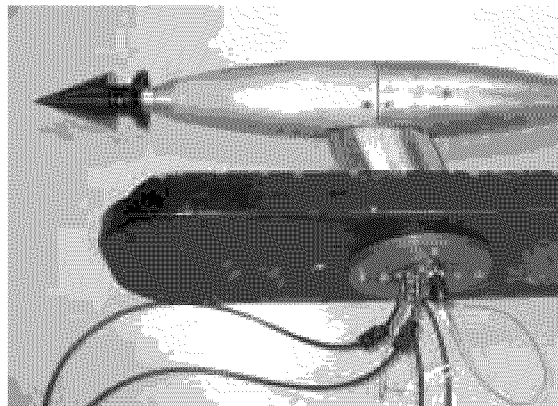

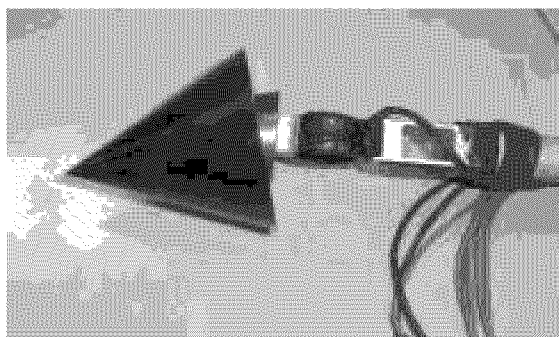Figure 28: Photograph of model for testing cavitators

Figure 29: Photograph of cavitator mounted on force cell balance

Photographs of cavities produced by conical and disk cavitators are shown in Figures (30 to 32). The differences in cavity appearance, by using continuous and stroboscopic lighting, are shown in Figures (30 and 31). Short exposure times, such as with stroboscopic lighting, should be used when investigating unsteady cavity dynamics. Strobe lights can be syncronized with the scanning rate of video systems to provide exposure times of a few microseconds for each video frame. The video record of the cavity can then be compared with transient measurements, such as forces, by use of a master clock. The photograph in Figure (32) shows a stable cavity and the effect of the strut mounting on the cavity. When investigating the downstream end of a cavity, a sting mount is used, or as shown in Figure (19) the cavitator can be supported with careful design of the struts.
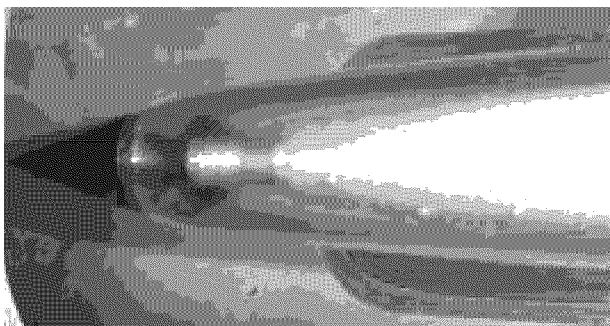

Figure 30: Photograph of cavity formed by a conical nosed cavitator- continuous lighting

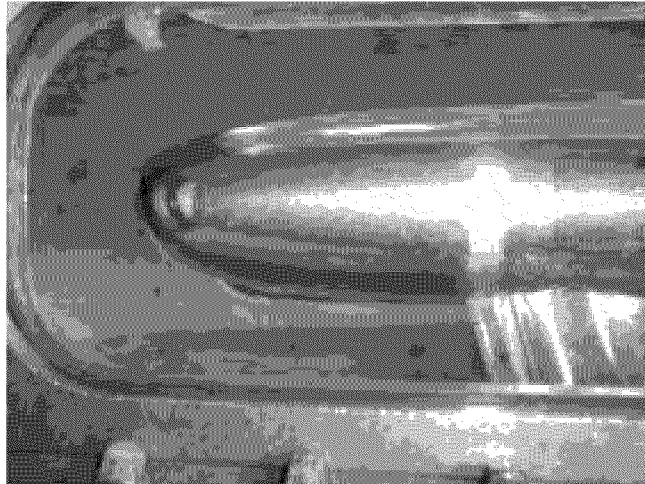Figure 31: Photograph of cavity formed by a conical nosed cavitator- stroboscopic lighting

Figure 32: Photograph of cavity formed by a disk at angle of attack

Cavity Piercing Hydrofoil/Control Surface Testing

Cavity piercing supercavitating hydrofoil/control surfaces have been tested in the ARL Penn State 12-inch diameter water tunnel. Some hydrofoils having wedge shaped cross sections are shown in Figure (33). The hydrofoil is mounted to a force balance and test fixture, as shown in Figure (34). The test fixture mounts through the water tunnel test section wall, and is designed so that there is a small gap between the base of the hydrofoil and the test section wall. The hydrofoil angle of attack can be adjusted by rotating the test fixture. A two-dimensional cavity is created along the test section wall upstream of the hydrofoil. This is done by ventilating downstream of a wedge mounted to the tunnel wall. The hydrofoil then pierces the tunnel wall cavity as shown in Figure (35). The wall cavity is approximately 25.4-mm (1.0-inch) thick at the leading edge of the hydrofoil. Reference lines are drawn along the hydrofoil, 25.4-and 38.1-mm (1.0 and 1.5-inches) from the base. The photograph in Figure (35) shows the pressure side view with the hydrofoil at high angle of attack. As shown in the figure, the tunnel wall cavity strikes the hydrofoil leading edge at the 25.4-mm (1.0-inch) reference line. The cavity along the hydrofoil surface is deflected down due to the constant pressure cavity and the pressure gradient along the surface. This deflection of the cavity changes the wetted area and affects the lift and drag forces. The hydrofoil cavity can be seen attached to the trailing edge in the figure.
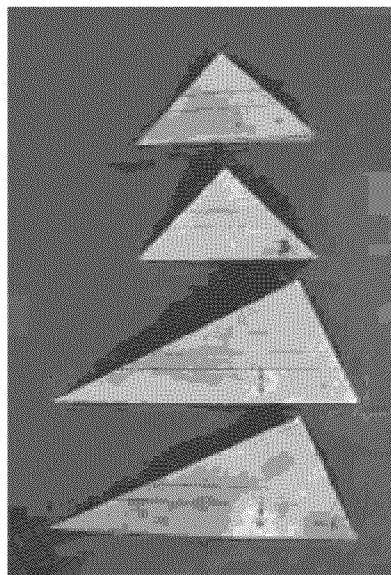

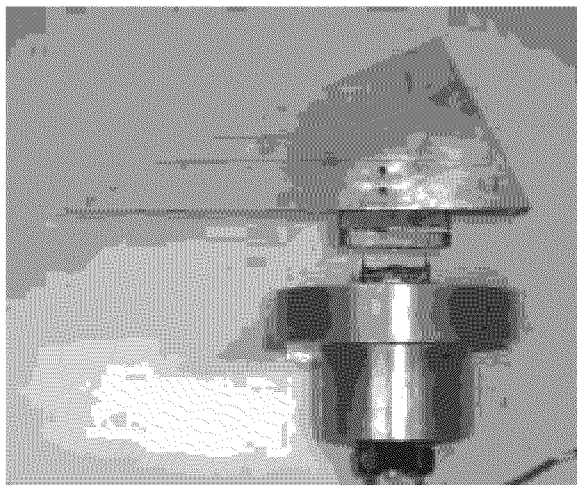Figure 33: Cavity piercing hydrofoils having wedge shaped cross sections

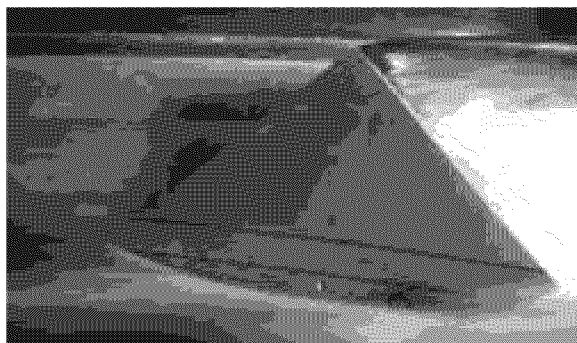Figure 34: Cavity piercing hydrofoil showing force balance and tunnel mounting fixture

Figure 35: Photograph of pressure side of cavity piercing hydrofoil

The suction side view of a hydrofoil at high angle of attack is shown in Figure (36). This view shows disturbances in the cavity wall due to imperfections along the hydrofoil leading edge. For a hydrofoil with a very sharp leading edge and at large angles of attack, the cavity is transparent and stable near the hydrofoil. At low angles of attack the cavity is attached at the base as shown in Figure (37), and is termed base cavitation. At intermediate angles of attack between base cavitation and supercavitation there can be what is termed partial cavitation. With partial cavitation there may be intermittent cavitation along the suction face, a small, attached cavity or a vortex cavity. Figure (38) shows the stable sheet cavity and supercavitating tip vortex formed by a higher aspect ratio hydrofoil. The forces associated with the different forms of hydrofoil cavitation will be discussed next.
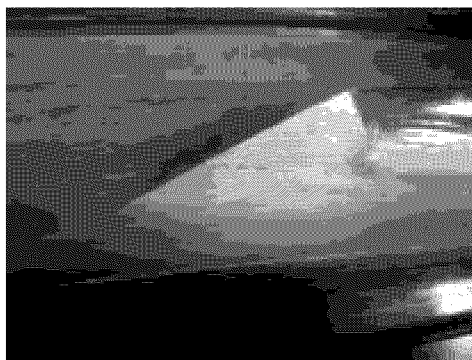

Figure 36: Photograph of suction surface of cavity piercing hydrofoil that shows
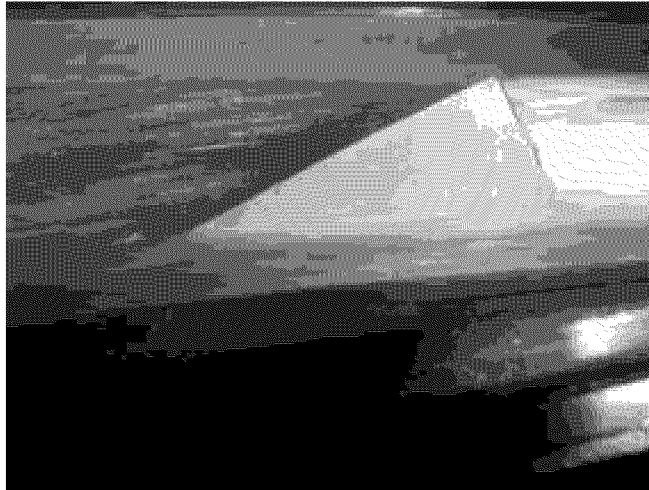cavity disturbances due to imperfections along leading edge.

Figure 37: Photograph of cavity piercing hydrofoil at low angle of attack, with base cavitation

Figure 38: Photograph of cavity from higher aspect ratio cavity piercing hydrofoil

Typical lift and drag coefficient curves as a function of angle of attack for a cavity piercing hydrofoil, are shown in Figure (39). The reference area for reducing forces to coefficient form was the wetted area if the tunnel wall cavity was not affected by the hydrofoil surface pressure gradient. The force coefficients have also been calculated based upon the actual wetted area, as determined from videotapes of the tests, see Figure (35). The complex shape of the force coefficient curves is due in part to the transitions between base, partial, and supercavitating flow regimes.

While the figure shows the averaged force coefficients, the time dependent forces due to cavity fluctuations can also be very important. Time dependent forces for base cavitation are shown in Figures (40 and 41), partial cavitation in Figures (42 and 43), and supercavitating conditions in Figure (44 and 45). For all figures, at time zero the hydrofoil is fully wetted. At approximately 1.25 seconds the tunnel wall cavity is established and the hydrofoil pierces the cavity. After establishment of the tunnel wall cavity, both lift and drag decrease for all conditions, as expected. The primary difference due to the changes in forms of cavitation can be seen in the lift plots. The lift for base cavitation and supercavitation show relatively little fluctuation. However, with partial cavitation there are large changes in lift. All tests in the tunnel were documented with video cameras using stroboscopic lighting synchronized with the video scanning. These changes in lift were associated with intermittent bursts of cavitation on the hydrofoil suction surface. In some cases the lift fluctuations were up to 50%.

For these fins with wedge shaped cross sections, the intermittent cavitation occurred when the relative flow direction near the leading edge was close to the wedge half-angle in the direction of flow. This relative flow direction is affected by the perturbation in the tunnel wall cavity due to the pressure side pressure gradient. The "effective half-angle" is then also affected by the cavity perturbation. Practical designs must take into consideration these factors that affect the unsteady cavity behavior.
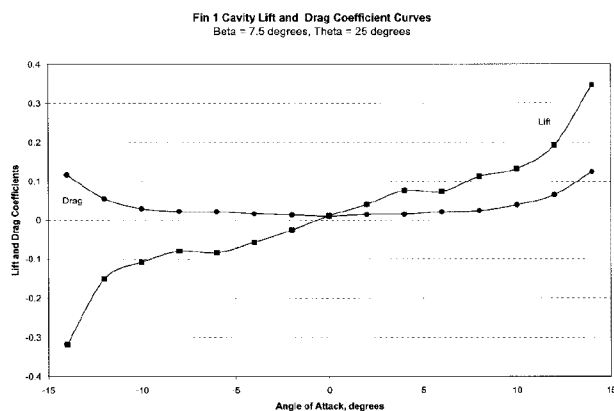

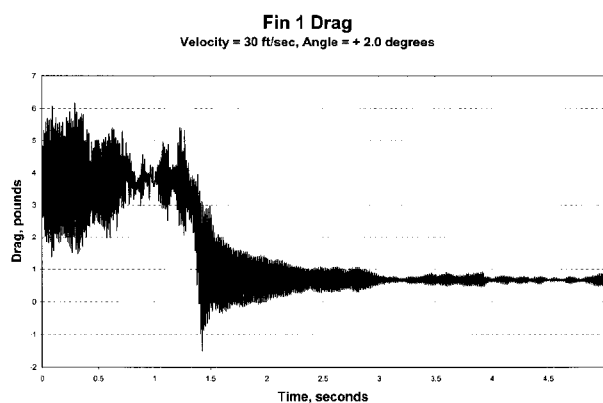Figure 39: Lift and drag coefficients for a cavity-piercing hydrofoil as a function of angle of attack

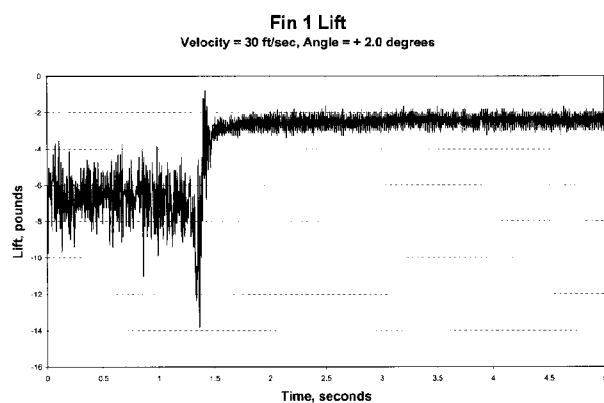Figure 40: Drag force as a function of time, base cavitation

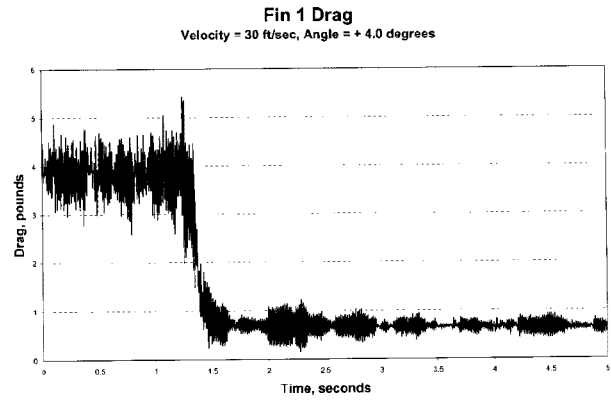Figure 41: Lift force as a function of time, base cavitation

Fin 1 Drag
Velocity = 30 ft/sec, Angle = + 4.0 degrees

Figure 42: Drag force as a function of time, partial cavitation

Fin 1 Lift
Velocity = 30 ft/sec, Angle = + 4.0 degrees
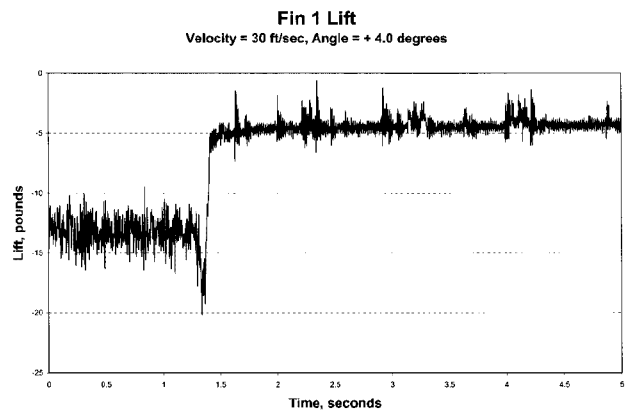
Figure 43: Lift force as a function of time, partial cavitation

Fin 1 Drag
Velocity = 30 ft/sec, Angle = + 10.0 degrees
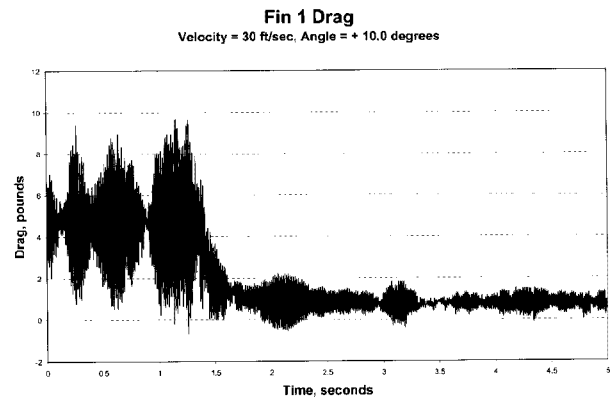
Figure 44: Drag force as a function of time, supercavitation

Fin 1 Lift
Velocity = 30 ft/sec, Angle = + 10.0 degrees
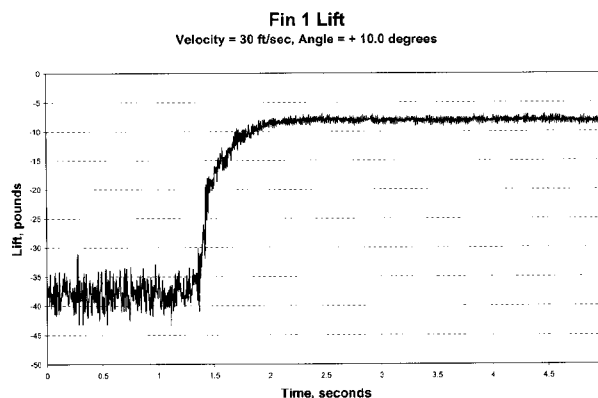

Figure 45: Lift force as a function of time, supercavitation

Summary

This report presents a summary of the cavitation flow regimes and experimental techniques used at ARL Penn State for investigating developed cavitation physics.

References:

1. Arakeri, V. H. and A. J. Acosta, "Viscous Effects in Inception of Cavitation on Axisymmetric Bodies," *J. of Fluids Engr.*, ASME, December 1973, pp. 519-526.

2. Gates, E. M. and M. L. Billet, "Cavitation Nuclei and Inception," IAHR Symposium, Tikyo, Japan, 1980, pp. 3-25.

3. Holl, J. W., R. E. A. Arndt, and M. L. Billet, "Limited Cavitation and the Related Scale Effects Problem, The Second international JSME Symposium on Fluid Machinery and Fluidics, Tokyo, Japan, 1972, pp. 303-314.

4. Stahl, H. A. and A. J. Stephanoff, "Thermodynamic Aspects of Cavitation in Centrifugal Pumps," *J. of Basic Engr.*, ASME, Vol 78, 1956, pp. 1691-1693.

5. Holl, J. W., M. L. Billet, and D. S. Weir, "Thermodynamic Effects on Developed Cavitation," *J. of Fluids Engr.*, Vol. 97, No. 4, Dec. 1975, pp. 507-514.

6. Billet, M. L., J. W. Holl, and D. S. Weir, "Correlations of Thermodynamic Effects for Developed Cavitation," *J. of Fluids Engr.*, Vol. 103, Dec. 1981, pp. 534-542.

7. Gilbarag, D., and J. Serrin, "Free Boundaries and Jets in the Theory of Cavitation," *J. of Math and Physics*, Vol 29, April 1950, pp. 1-12.

8. Stinebring, D. R., M. L. Billet, and J. W. Holl, "An Experimental Study of Cavity Cycling for Ventilated and Vaporous Cavities," International Symposium on Jets and Cavities, ASME, Miami Beach, FL, Nov. 1985, pp. 1-4.

9. Ward, R. L., "Cavity Shapes for Circular Disks at Angles of Attack," CA Inst. of Tech. Hydrodynamic Lab Report, E-73.4, 1957.

10. Swanson, W. M., and J. P. O'Neill, "The Stability of an Air-Maintained Cavity Behind a Stationary Object in Flowing Water," Hydrodynamic laboratory, CA Inst. of tech, M24.3, Sept 1951.

11. Cox, R. N. and W. A. Clayden, "Air Entrainment of the Rear of a Steady Cavity," Symposium on Cavitation in Hydrodynamics, National Physical Laboratory, Sept. 1955.

12. Ward, R. L., "Experimental Investigation of Forced Ventilated Cavities on Hydrofoils of Various Chord Lenths," Report No. LMSC/D243664, Lockheed Missiles and Space Corp, Sunnyvale, CA, Dec. 1968.

13. Billet, M. L. and D. S. Weir, "The Effect of Gas Diffusion on the Flow Coefficient for a Ventilated Cavity," *J. of Fluids Engr.*, ASME, Vol. 97, Dec. 1975, pp. 501-506.

14. Brennen, C., "The Dynamic Balances of Dissolved Air and Heat in Natural Cavity Flows," *J. of Fluid Mechanics,* Vol. 37, Part 1, 1969, pp. 115-127.

15. Stinebring, D. R., and J. W. Holl, "Water tunnel Simulation Study of the Later Stages of Water Entry of Conical Head Bodies: Phase II – Effect of the Afterbody on Steady State Ventilated Cavities," ARL Penn State Report No. TM-79-206, Dec. 1979.

16. May, A., "Water Entry and the Cavity-Running Behavior of Missiles," *SEAHAC Technical Report 75-2*, Naval Surface Weapons Center, White Oak Laboratory, Silver Spring, MD, 1975.

17. Logvinovich, G., "Hydrodynamics of Free-Boundary Flows," *Trudy TsAGI,* 1980.

18. Knapp, R. T., J. W. Daily, and F. G. Hammitt, "Cavitation," McGraw-Hill, 1970.